Formation of Y_2O_3 nanoclusters in nanostructured ferritic alloys during isothermal and anisothermal heat treatment: A kinetic Monte Carlo study

C. Hin,[1,2] B. D. Wirth,[1] and J. B. Neaton[3]
[1]*Department of Nuclear Engineering, University of California, Berkeley, California 94720-1730, USA*
[2]*Department of Materials Sciences and Engineering, Massachusetts Institute of Technology, Cambridge, Massachusetts 02139-4307, USA*
[3]*Molecular Foundry, Lawrence Berkeley National Laboratory, Berkeley, California 94720-1730, USA*
(Received 12 February 2009; revised manuscript received 28 September 2009; published 21 October 2009)

Kinetic Monte Carlo simulations, based on parameters obtained with density-functional theory in the local-density approximation and experimental data, are used to study bulk precipitation of Y_2O_3 in α iron. The simulation involves realistic diffusion mechanisms, with a rapid diffusion of O atoms by interstitial jumps and a slower diffusion of Fe and Y atoms by vacancy jumps, and a point defect source which drives the vacancy concentration toward its equilibrium value, during isothermal and anisothermal heat treatments. Depending on alloy and thermal history conditions, the Monte Carlo simulations predict different kinetic behavior, including transient precipitation of metastable iron oxides followed by precipitation of Y_2O_3 nanoclusters.

DOI: 10.1103/PhysRevB.80.134118 PACS number(s): 61.82.Bg

I. INTRODUCTION

The improvement of creep resistance is a principal objective for use of advanced ferritic alloys in applications at high temperatures and in extreme environments. Conventional oxide-dispersion strengthened alloys are the prototypical materials and microstructures for improved creep resistance in high-temperature energy-production applications.[1–7] However, experiments show that a high-number density of nanoscale Y-Ti-O precipitates can also improve creep resistance. It is also believed that the Y-Ti-O clusters, in addition to impeding dislocations and reducing grain-boundary mobility, act as traps for insoluble helium that would be generated in fusion reactor structural components. This is an example where atomic scale processes over nanometer lengthscales and 10^6 s time scales can dictate macroscopic properties such as creep and reliability. Monte Carlo methods provide an efficient approach for investigating kinetic processes of precipitation as well as the structure and morphological evolution of Y-Ti-O clusters in these advanced ferritic alloys. Simulations, such as those presented in this paper, illuminate precipitate formation and composition evolution processes that must be incorporated in models of processing and reliability.[8,9]

The aim of this study is to understand the kinetic path of Y_2O_3 nanoparticles in ferrite by Kinetic Monte Carlo (KMC) simulations during an anisothermal heat treatment, which is characteristic of the thermal processing of advanced ferritic alloys. This Fe-Y-O system has been recently studied both experimentally[6,7] and computationally.[10] The results of these works and this present study will provide a foundation for further study to investigate the kinetic precipitation pathway in quaternary Fe-Ti-Y-O alloys.

Y_2O_3 has a c-type cubic crystal structure, characteristic of the rare-earth oxides (space group *Ia*3). This phase of Y_2O_3 can be understood as the CaF2 structure with a doubling of the CaF2 lattice parameter and with a quarter of the anions removed. The experimental lattice constant is 1.0604 nm.[11] Due to the lattice mismatch, Y_2O_3 precipitates must be incoherent with the α-iron matrix, which is body-centered cubic (bcc) with a lattice parameter of 0.287 nm. However, during aging time, the small and flat precipitates are expected to retain partial coherency. Unfortunately, this assumption has yet to be verified by high-resolution electron microscopy. On the other hand, several past experimental studies have reported on the evolution of the number density, size, and composition of Y_2O_3 precipitates above 1 nm.[6,7] This provides a means for comparison with analytical models, which in turn can provide information on the initial stages of nucleation, which is poorly understood.

It is typical to study precipitation kinetics with numerical models based on the classical theory of nucleation, growth, and coarsening.[10,12–14] In these approaches, different kinetic regimes usually overlap and have been treated in a unified model of homogeneous precipitation of Y_2O_3 in ferrite during an anisothermal heat treatment.[10] By a suitable choice of fitting parameters, such as the interfacial free energy, the solubility product, and the diffusion coefficient of Y in ferrite, this model has reproduced well the experimental evolutions of the number and size of precipitates during the growth and coarsening stages.[10] However, the nucleation stage cannot be directly compared due to a lack of experimental data. Nevertheless, these models rely on simplifying assumptions, such as: the precipitates are spherical and stoichiometric; the interfacial free energy is independent of temperature and precipitate size; and the precipitation kinetics is limited by the diffusion of yttrium, which is much slower than the diffusion of oxygen. KMC simulations, which are based on the description of the atomic diffusion mechanisms that control precipitation, do not make such assumptions.

In the next section, the diffusion model and the Monte Carlo algorithm developed in this work are presented. The KMC simulations are performed on a rigid bcc lattice, with oxygen atoms placed on the octahedral sites and Fe or Y atoms placed on substitutional sites. Thus, the diffusion of Fe, Y, and O atoms occurs by a realistic mechanism, which involves a vacancy or interstitial jump. A vacancy source and sink is also introduced, which drives the concentration of vacancies toward the equilibrium value for a given temperature condition. This enables the study of precipitation kinet-

ics under conditions associated with anisothermal heat treatment, which may be important in understanding the high-number density of nanoscale Y_2O_3 precipitates, partially responsible for the improved creep strength of advanced ferritic alloys. The details of the determination of the parameters (pair interaction energies, attempt frequencies, saddle-point binding energies) by fitting to first-principles calculations and experimental data of Fe-Y-O alloys, are also provided in this section. The results of the Monte Carlo simulations are presented in Sec. III, where in particular, the effects of anisothermal and isothermal heat treatment are compared, and the impact of supersaturation of the initial solid solution on the kinetic pathway are discussed.

II. NUMERICAL METHOD

A. Crystallographic model

Y_2O_3 has a c-type cubic crystal structure, common among rare-earth oxides (space group $Ia3$). The ground-state atomic arrangement of Y_2O_3 can be understood by starting with the CaF2 structure, then doubling the lattice parameter and removing a quarter of the anions. The lattice constant is 1.0604 nm (Ref. 11) with the unit cell containing 48 oxygen and 32 yttrium ions.

Even assuming that the Y_2O_3 phase is coherent with the ferrite matrix for small precipitate size, when the precipitates grow, the lattice mismatch between the Y_2O_3 phase and the iron matrix is up to 50% and Y_2O_3 becomes fully incoherent with the iron matrix. However, since the precipitate size remains very small in our simulations (with a radius always less than 0.6 nm), it is reasonable to assume that the precipitates are coherent. Since the structure of the coherent transition phase is unknown, assumptions are required in order to simulate the homogeneous precipitation of Y_2O_3 in ferrite by KMC simulation on a rigid lattice.

The KMC model uses a rigid lattice model with simple cubic symmetry and a lattice parameter of $a/2$, where a is the lattice parameter of α iron. This lattice has been divided into three sublattices: one sublattice is occupied by Fe and Y atoms and vacancies, which is referred to as the "substitutional" lattice (atoms in gray in Fig. 1), and two other sublattices correspond to octahedral interstitial sites for oxygen atoms (in white in Fig. 1). A stoichiometric Y_2O_3 phase coherent with the iron bcc lattice may be constructed from this lattice, with yttrium atoms on the substitutional sites and oxygen atoms occupying 1/2 of the interstitial sites. The Y_2O_3 phase may be built up two different ways as illustrated in Fig. 1. In this structural model, the possible atomic arrangements are strongly constrained. However, this approximation is acceptable because the elastic contribution to the free energy is implicitly considered through the fact that the correct precipitation driving force of the Y_2O_3 phase in ferrite is reproduced by fitting the Y-O interactions from the experimentally determined solubility product.

B. Atomistic kinetic model

The simulated crystal is constructed on a rigid bcc lattice with full periodic boundary conditions. Fe and Y atoms and vacancies are distributed among substitutional sites of the rigid bcc lattice. O atoms are distributed among the octahedral interstitial sites of the bcc lattice. Species Fe, Y, and O situated on nth neighbor sites of the simple cubic lattice, interact via pair interaction energies $\varepsilon_{\mathrm{FeFe}}^{(n)}$, $\varepsilon_{\mathrm{FeY}}^{(n)}$, $\varepsilon_{\mathrm{YY}}^{(n)}$, $\varepsilon_{\mathrm{FeO}}^{(n)}$, $\varepsilon_{\mathrm{YO}}^{(n)}$, and $\varepsilon_{\mathrm{OO}}^{(n)}$. The first nearest-neighbor interaction energy $\varepsilon_{\mathrm{OV}}^{(1)}$ between a vacancy and oxygen, and third nearest-neighbor interaction energies $\varepsilon_{XV}^{(3)}$ between vacancy and atoms X (X=Fe or Y) are also introduced in order to take into account the strengthening of chemical bonds of less coordinated atoms.[15] The energy of the system is assumed to be the sum of pair interaction energies. For low concentration, the equilibrium properties of the system are not affected by the vacancy, and the energy of the system is given by

$$E = \sum_{n,i,j} N_{ij}^{(n)} \varepsilon_{ij}^{(n)}, \tag{1}$$

where $N_{ij}^{(n)}$ is the number of nth neighbor ij pairs. The interaction energies are provided in Table I, and described in more detail in Sec. II D.

We described the kinetics in this ternary alloy with the following model:[16] (1) the diffusion of Fe and Y atoms occurs by a mechanism in which atoms exchange position with a vacancy V located on first nearest-neighbor sites of the bcc lattice (third nearest-neighbor sites of the simple cubic lattice), (2) oxygen atoms can diffuse directly onto any of the free nearest-neighbor octahedral sites, and (3) the jump frequency is a thermally activated process.

The jump frequencies are given by

$$\Gamma_{XV} = \nu_X^0 \exp\left\{-\frac{\Delta E_X}{kT}\right\} \tag{2}$$

for substitutional atoms (X=Fe or Y) and by

$$\Gamma_{OV} = \nu_O^0 \exp\left\{-\frac{\Delta E_O}{kT}\right\} \tag{3}$$

for oxygen atoms (in this case X=O).

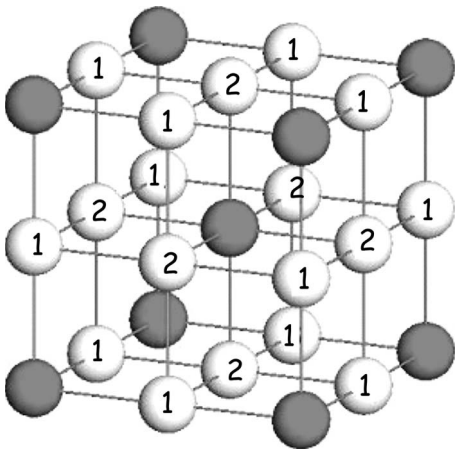

FIG. 1. Lattice model used for the simulation of Fe-Y-O alloys. The sublattice of α iron corresponds to the black spheres; O atoms (white) form another sublattice by filling one of the two numbered variants. One cell of the simple cubic lattice corresponds to 1/8 of the bcc structure.

TABLE I. Pair interaction energies of the Fe-Y-O system on the simple cubic lattice.

	i-j interactions (eV)			
Fe-Fe			−0.65	−0.65
Y-Y			0.31	−0.57
Fe-Y			−0.46	−0.42
O-O	+0.10	−0.116	+0.10	−0.116
Fe-O	−0.19	−0.19		
Y-O	−0.90	−0.45		
Fe-V			−0.21	0
Y-V			−0.35	0
O-V	−0.31	0		
V-V			−0.20	+0.42

The pre-exponential factors ν^0 are the attempt frequencies, which are assumed to depend on the nature of the atoms X but not on the alloy configuration. T is the temperature, and k is the Boltzmann constant. The activation energy ΔE_X is the energy required to extract the jumping species from their local environment minus the energy recovered by placing the jumping atom at the saddle point. Thus, the activation energy is given by

$$\Delta E_X = e_X^{SP} - \sum_{n,i} \varepsilon_{Xi}^{(n)} - \sum_{n,j} \varepsilon_{Vj}^{(n)}, \tag{4}$$

where the sums of the pair interaction energies, $\Sigma_{n,i}\varepsilon_{Xi}^{(n)}$ and $\Sigma_{n,j}\varepsilon_{Vj}^{(n)}$, are performed over the neighboring sites of the jumping atom X and V (V being able to be the vacancy or the free interstitial site). e_X^{SP} is a "saddle-point binding energy," which corresponds to the interaction of the atom X with the neighboring atoms when it is at the saddle point between its initial and final positions. The numerical value of e_X^{SP} affects the kinetics of the system but not its thermodynamic properties. In this study, as for the attempt frequency, the saddle-point contribution e_X^{SP} only depends on the nature of jumping species but not on the configuration. However, it is important to note that even if e_X^{SP} is independent of the configuration, the activation energy ΔE_X depends on the local environment.

C. Residence time algorithm

1. Time scale

Our KMC algorithm is described as follows. At each Monte Carlo step, for the substitutional case, a vacancy can undergo z exchanges with its nearest neighbors. For the interstitial case, an oxygen atom can exchange its site with z' free interstitial sites. One of these exchanges is chosen according to the residence time algorithm described in Ref. 17. The physical time associated with each Monte Carlo step is given by

$$t_{MCS} = \left(\sum_{i}^{i=z\times N_v} \Gamma_i + \sum_{j}^{j=N_O\times z'} \Gamma_j \right)^{-1}, \tag{5}$$

where N_O is the number of oxygen atom in the simulation box.

2. Vacancy source and sink

In most of the KMC simulations of phase transformations which consider diffusion by point defects, the point defect concentration is kept constant (usually one or a few vacancies in the simulation box). In simulation boxes of a few millions of atoms or less, the corresponding vacancy concentration ($C_V^{eq} \sim 10^{-6}$) is thus usually much higher than the equilibrium one: for a vacancy formation energy of $E_V^{for}(\mathrm{Fe}) = 2.24$ eV in iron, one gets $C_V^{eq} = 6.7 \times 10^{-23}$ at 500 K, $C_V^{eq} = 5.2 \times 10^{-12}$ at 1000 K. The overestimation of the vacancy concentration in the simulation box leads to the acceleration of the diffusion coefficients of the elements on the substitutional sites. A rescaling of the time is then needed in order to get a physical time scale, which is usually based on the assumption that the precipitation kinetics is sufficiently slow so that the vacancy concentration always remains at its equilibrium value (see, e.g., Ref. 18). The rescaling of time can be done by changing the diffusion coefficients of the yttrium and the iron atoms via their attempt frequencies relative to the atom-vacancy exchanges. ν_{Fe} and ν_{Y} can then be written as

$$\nu_X^0 = \frac{D_X^0}{f_0 a^2} \times \frac{c_v^{eq}}{c_V^{simu}} = \frac{D_X^0}{f_0 a^2} \times \exp\left(-\frac{E_V^{for}}{kT} \right) \frac{N_S}{N_V}, \tag{6}$$

where D_X^0 is the pre-exponential factor, f_0 is the correlation factor, c_V^{simul} is the vacancy concentration in the simulation box, E_V^{for} is the vacancy formation energy in iron, N_V is the number of vacancy in the simulation box and N_S is the number of substitutional sites.

This assumption (fixed number of vacancies) and this rescaling of time, can be avoided with the method developed and used in many works.[8,13,19] A vacancy "source/sink" is introduced on a given site of the iron matrix. A vacancy is created on that source and is positioned on one of the $z_3 = 8$ nearest-neighbor sites of the bcc lattice with a frequency

$$\Gamma_V^+ = z_3 \nu_{\mathrm{Fe}}^0 \exp\left\{ -\frac{E_V^{for}(\mathrm{Fe}) + Q}{kT} \right\}. \tag{7}$$

Conversely, during its diffusion in the crystal, when a vacancy reaches one of the sites surrounding the source, it can jump on this site and disappear with a frequency

$$\Gamma_V^- = \nu_{\mathrm{Fe}}^0 \exp\left\{ -\frac{Q}{kT} \right\}. \tag{8}$$

Q is the vacancy migration barrier between the source/sink and its neighbors. This parameter controls the efficiency of the source and the kinetics of vacancy formation. Our KMC simulations have been done with $Q = 0.6$ eV. We have confirmed that with this value, the vacancy concentration evolves rapidly toward its equilibrium concentration, the number of vacancies in the simulation boxes varying from

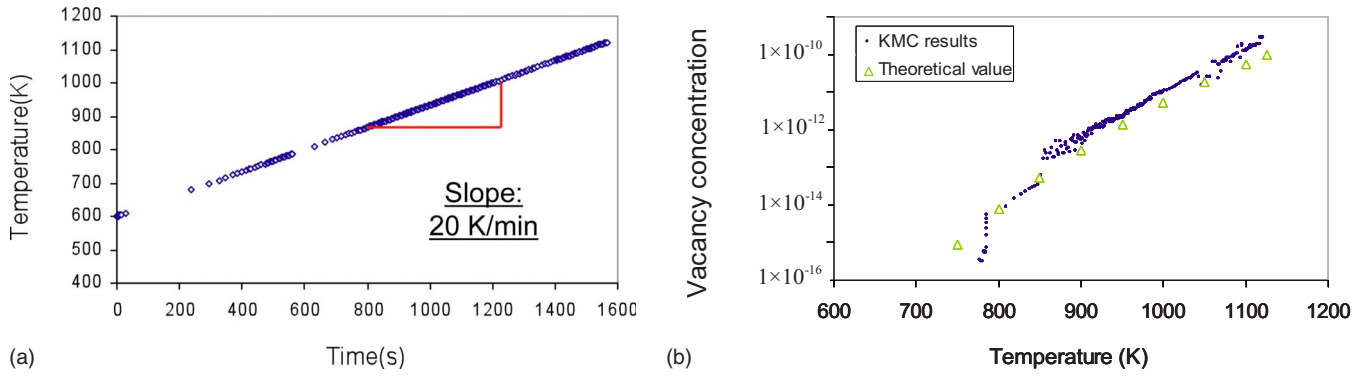

FIG. 2. (Color online) (a) Evolution of temperature as a function of time during an anisothermal heat treatment. The temperature ramp rate is equal to 20 K/min, up to a maximum temperature of 1125 K. The alloy is composed of Fe-0.124 at. %Y-0.186 at. %.O. The simulation box is comprised of $100\times100\times100$ bcc cells. (b) Evolution of vacancy concentration as a function of temperature during an anisothermal heat treatment. The temperature ramp rate is equal to 20 K/min, up to a maximum temperature of 1125 K. The alloy is composed of Fe-0.124 at. %Y-0.186 at. %.O. The simulation box is comprised of $100\times100\times100$ bcc cells.

zero to one vacancy throughout the simulation.

In the simulation, the creation or annihilation of vacancies are processed by the residence time algorithm as an additional event with its own frequency. Compared with an algorithm where the number of vacancies remains constant throughout the simulation, the advantage of the above method is that the system can have, averaged over time, the equilibrium density of vacancies, which continuously varies with temperature.

3. Temperature ramp

The introduction of a source and sink in this KMC algorithm automatically drives the vacancy concentration toward its equilibrium value whatever the temperature. This provides the ability to explore the effect of anisothermal heat treatments. Experimental processing treatments typically consist of a temperature ramp rate of 20 K/min, up to 1125 K and then the temperature is maintained for 200 min.[7]

At each Monte Carlo step, the time t is determined according to Eq. (5) and the temperature T is recalculated according to the thermal process as

$$T = at + b. \tag{9}$$

In our case, $a=20$ K/min and b is the initial temperature of the simulation (e.g., 600 K). Below 600 K, the diffusion coefficients of the different species are too small to observe an influence on the kinetics of precipitation.

During the KMC simulation, when the temperature difference becomes greater than 0.2 K, all the frequencies are updated according to the new temperature (e.g., the jump frequencies and the vacancy emission frequency). When the temperature plateau is reached (e.g., at 1125 K), the frequencies are updated a final time as a function of temperature. This procedure has been tested in a system with relatively low supersaturation (Fe-0.12 at. %Y-0.18 at. %O) and $100\times100\times100$ bcc cells. One observes that this procedure ensures the quasicontinuity of the temperature ramp [Fig. 2(a)] and the evolution of the vacancy concentration [Fig. 2(b)], which has been compared to the theoretical value given by

$$c_v^{eq} = \exp\left(-\frac{E_V^{for}(\mathrm{Fe})}{kT}\right). \tag{10}$$

The vacancy formation energy in iron $E_V^{for}(\mathrm{Fe})$ was determined by first-principles calculations as described in the next section and found to be equal to 2.24 eV.

This procedure is critical to correctly model the vacancy diffusion and correspondingly, the kinetic precipitation path during anisothermal heat treatment. Similar results are obtained for different degree of supersaturations.

D. Parameterization

1. Thermodynamic parameters

In the framework of the rigid lattice approximation used in the simulations, the equilibrium properties of the Fe-Y-O alloys depends on the pair interactions $\varepsilon_{ij}^{(n)}$ between component i and j located on the nth nearest-neighbor sites (on the simple cubic lattice with a lattice parameter $a/2$). Interactions up to the fourth neighbors have been used and are summarized in Table I. As can be seen, there are no interactions between substitutional atoms (Fe or Y) for the first and second neighbor distances which correspond to interstitial sites. Because of the simplicity of the lattice model, we cannot reproduce the true crystalline structure of the O-rich (e.g., FeO) and Y-rich (e.g., $Fe_{17}Y_2$) phases in equilibrium with α iron. They are respectively replaced by a quadratic centered Fe_2O_3 phase and a B2 (CsCl-type) FeY phase. Nevertheless, the O and Y solubility limits of the model have been fit to the experimental ones, in order to keep the good precipitation driving force.

The parameters are fit to thermodynamic experimental properties of Fe-Y-O, Fe-Y and Fe-O alloys. Pair interaction energies $\varepsilon_{\mathrm{FeO}}^{(n)}$, and cohesive properties are calculated by first-principles calculations. All the free-energy calculations are performed using first-principles density-functional theory in the local density approximation, with the Ceperley-Alder form for the correlation energy as parameterized by Perdew and Zunger[20] and with ultrasoft Vanderbilt-type pseudopotentials.[21] All calculations were performed with the VASP

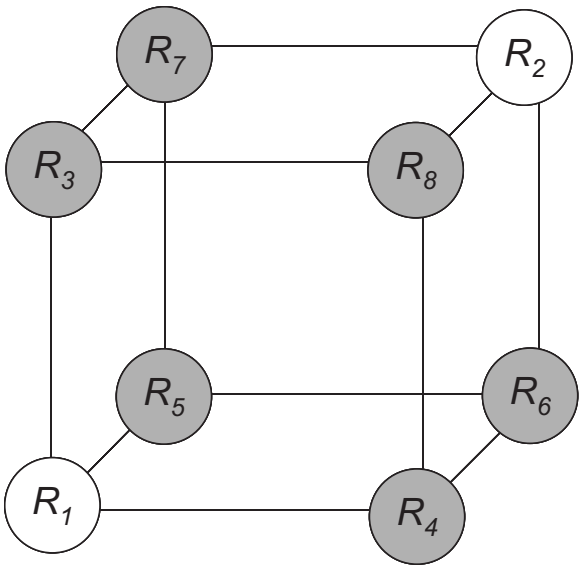

FIG. 3. Decomposition of the lattice in eight sublattices used to determine the free energy of the Fe-Y-O system. Sites 1 and 2 are the substitutional sites for yttrium and iron atoms. Sites 3–8 are the interstitial sites for oxygen atoms.

package. Calculations were done at zero temperature and pressure and without zero-point motion. The energy cutoff in an alloy was set to 1.5 times the larger of the suggested energy cutoffs of the pseudopotential of the element of the alloy (e.g., 401.95 eV in pure iron and 317.70 eV in pure yttrium). This suggested energy cutoffs are derived by the method described in Ref. 22. Brillouin zone integration was performed using $12\times12\times12$ k points distributed uniformly on a Monkhorst-Pack mesh.[23,24] Since α iron is a magnetic alloy, spin polarization was used. All the structures were fully optimized.

The $\varepsilon^{(1)}_{\mathrm{FeO}}$ interaction has been determined by calculating the total energy with 54 iron atoms minus the total energy with 54 iron atoms and one oxygen atom in interstitial position. $\varepsilon^{(2)}_{\mathrm{FeO}}$ is assumed to have the same value as $\varepsilon^{(1)}_{\mathrm{FeO}}$.

The $\varepsilon^{(n)}_{\mathrm{FeFe}}$ interactions have been fit to the iron cohesive energy calculated from first-principles calculations, according to $E_{coh}(\mathrm{Fe})=\frac{z_3}{2}\varepsilon^{(3)}_{\mathrm{FeFe}}+\frac{z_4}{2}\varepsilon^{(4)}_{\mathrm{FeFe}}$. $\varepsilon^{(n)}_{\mathrm{YY}}$ has also been fit to the cohesive energy of the yttrium bcc structure obtained from first-principles calculations.

Using the Bragg-Williams approximation,[25,26] the $\varepsilon^{(4)}_{\mathrm{FeY}}$ interaction has been fit to reproduce the yttrium solubility limit in iron.[27] The mean-field approximation leads to dividing the rigid lattice in sublattices characterized by the number of occupation in each species. For the Fe-Y-O system, we used the same lattice as for the KMC simulations, i.e., a simple cubic lattice of parameter $a/2=1.435$ Å including eight atoms on apexes. As shown in Fig. 3, iron and yttrium atoms are located on substitutional sites (R_1 and R_2) and oxygen atoms are located on the interstitial sites ($R_3\rightarrow R_8$). c_i are the concentrations on the lattice R_i, with $i=1$ or 2 for yttrium atoms and $i\in\{3,8\}$ for oxygen atoms. Since the vacancy concentration is very small, we assume that substitutional lattice sites are only occupied by iron or yttrium atoms. Consequently, the iron concentrations on substitutional sites are $1-c_1$ and $1-c_2$. Nominal concentrations for each element as a function of concentration on different sublattices are

$$c_{\mathrm{Fe}}=\frac{(1-c_1)+(1-c_2)}{2+\sum_{i=3}^{8}c_i},\quad c_{\mathrm{Y}}=\frac{c_1+c_2}{2+\sum_{i=3}^{8}c_i},\quad \text{and}\quad c_{\mathrm{O}}=\frac{\sum_{i=3}^{8}c_i}{2+\sum_{i=3}^{8}c_i}. \tag{11}$$

Keeping the quadratic part, the internal energy per lattice is

$$\begin{aligned}U=&\,2\Omega_3c_1c_2+\Omega_4(c_1^2+c_2^2)+2W_1[c_1(c_3+c_4+c_5)\\&+c_2(c_6+c_7+c_8)]+4W_2[c_1(c_6+c_7+c_8)\\&+c_2(c_3+c_4+c_5)]+2V^1_{CC}[c_3(c_7+c_8)+c_4(c_6+c_8)\\&+c_5(c_6+c_7)]+4V^2_{CC}[c_3c_4+c_3c_5+c_4c_5\\&+c_6c_7+c_6c_8+c_7c_8]+8V^3_{CC}[c_3c_6+c_4c_7+c_5c_8]\\&+3V^4_{CC}[c_3^2+c_4^2+c_5^2+c_6^2+c_7^2+c_8^2],\end{aligned} \tag{12}$$

where

$$\begin{aligned}\Omega_3&=4(\varepsilon^{(3)}_{\mathrm{FeFe}}+\varepsilon^{(3)}_{\mathrm{YY}}-2\varepsilon^{(3)}_{\mathrm{FeY}})\\\Omega_4&=3(\varepsilon^{(4)}_{\mathrm{FeFe}}+\varepsilon^{(4)}_{\mathrm{YY}}-2\varepsilon^{(4)}_{\mathrm{FeY}})\\W_1&=\varepsilon^{(1)}_{\mathrm{YO}}-\varepsilon^{(1)}_{\mathrm{FeO}}\\W_2&=\varepsilon^{(2)}_{\mathrm{YO}}-\varepsilon^{(2)}_{\mathrm{FeO}}.\end{aligned} \tag{13}$$

In addition, we assumed that the entropy can be reduced as a first approximation to the configurational entropy, which calculated per unit lattice is equal to

$$S=-k\sum_{i=1}^{8}[c_i\ln c_i+(1-c_i)\ln(1-c_i)]. \tag{14}$$

Equilibrium between the solid solution and the precipitate is calculated by considering the grand canonical free-energy function $A=F-\Sigma_i\mu_ic_i$, where $F=U-TS$. For each phase, this function is minimized for a given alloy chemical potential μ. The equilibrium potential is the one for which the minima A are the same for the solid solution and the precipitate phase. This problem can be solved analytically by considering the first-order Taylor expansion of the grand potential. For example, for the Fe-rich phase, we find

$$A_{\mathrm{Fe}}\sim0$$

$$\frac{\partial A_{\mathrm{Fe}}}{\partial c_1}\sim kT\ln c_1-\mu_Y=0$$

$$\frac{\partial A_{\mathrm{Fe}}}{\partial c_3}\sim kT\ln c_3-\mu_0=0$$

$$c_1=c_2$$

$$c_3 = c_4 = c_5 = c_6 = c_7 = c_8, \tag{15}$$

where μ_Y and μ_O are the yttrium and the oxygen chemical potential respectively. For the B2 FeY phase, we find

$$A_{FeY} \sim \Omega_4 - \mu_Y$$

$$\frac{\partial A_{FeY}}{\partial c_1} \sim 2\Omega_4 - kT\ln(1-c_1) - \mu_Y = 0$$

$$\frac{\partial A_{FeY}}{\partial c_2} \sim 2\Omega_3 + kT\ln c_2 - \mu_Y = 0$$

$$\frac{\partial A_{FeY}}{\partial c_3} \sim kT\ln c_3 - \mu_0 = 0$$

$$c_3 = c_4 = c_5 = c_6 = c_7 = c_8. \tag{16}$$

To determine the equilibrium between the ferrite and the FeY phase, we solve the system of Eqs. (15) and (16), where the unknowns are the concentration on each sublattice in both phase and the chemical potential μ_Y. By equalizing, A_{Fe} and A_{FeY}, we find

$$c_Y^{Fe} = 1 \times \exp\left(\frac{\Omega_4}{kT}\right) = 1 \times \exp\left(3\frac{(\varepsilon_{FeFe}^{(4)} + \varepsilon_{YY}^{(4)} - 2 \times \varepsilon_{FeY}^{(4)})}{kT}\right). \tag{17}$$

In order to reproduce phase separating Fe/FeY domain, the third nearest-neighbor order energy Ω_3 has been arbitrarily set to be greater than 0. Knowing $\varepsilon_{FeFe}^{(3)}$ and $\varepsilon_{YY}^{(3)}$ interactions, $\varepsilon_{FeY}^{(3)}$ has been fit to satisfy the condition $\Omega_3 > 0$.

As mentioned by Bhadeshia,[28] the partition function only depends on the repartition of atoms in the interstitial site of a matrix. Consequently, the only interactions which intervene in the calculation of the solubility limit of oxygen in ferrite are those between oxygen atoms. Applying the same method described above for the determination of the solubility limit of yttrium in ferrite, we find a solubility limit of oxygen in ferrite equal to

$$c_O^{Fe} = 2 \times \exp\left(\frac{4\varepsilon_{OO}^{(2)} + 3\varepsilon_{OO}^{(4)}}{kT}\right), \tag{18}$$

where $\varepsilon_{OO}^{(2)}$ and $\varepsilon_{OO}^{(4)}$ have been fit to the experimental value of the oxygen solubility limit in ferrite given in Ref. 29. Finally, in order to obtain a two-phase Fe/Fe_2O_3 domain, $\varepsilon_{OO}^{(1)}$ and $\varepsilon_{OO}^{(3)}$ must be positive.

The solubility product of Y_2O_3 in ferrite has been determined by fitting a classical nucleation-growth-coarsening model to small-angle neutron scattering data obtained by Allinger,[7] which provides the evolution of the number and size of Y_2O_3 precipitates as a function of time. The solubility product has been estimated to be

$$K_s^{Y\text{-}O} = \exp\left(\frac{-29\,200}{T} + 1.33\right). \tag{19}$$

For example, at 1000 K, the solubility product is equal to 2×10^{-11}. The low value of the solubility product has the effect of accelerating the nucleation and the growth stage, and slowing down the coarsening stage of the Y_2O_3 precipitation kinetics. Once again, the same method described above to determine the solubility of both yttrium and oxygen in ferrite is applied. The equilibrium between ferrite and yttrium oxides is controlled at low temperature by the quantity

$$K_s^{Y\text{-}O} = 2 \times \exp\left(\frac{\Omega_3 + \Omega_4 + \frac{5}{2}(\varepsilon_{YO}^{(1)} - \varepsilon_{FeO}^{(1)}) + 5(\varepsilon_{YO}^{(2)} - \varepsilon_{FeO}^{(2)}) + 4\varepsilon_{OO}^{(2)} + 3\varepsilon_{OO}^{(4)}}{kT}\right). \tag{20}$$

From this solubility product, $\varepsilon_{YO}^{(1)}$ and $\varepsilon_{YO}^{(2)}$ are evaluated. In order to reproduce the Y_2O_3 phase, $\varepsilon_{YO}^{(1)}$ must be twice as large as $\varepsilon_{YO}^{(2)}$.

Vacancy-atom interactions $\varepsilon_{XV}^{(n)}$ and vacancy-vacancy interactions are also considered. Vacancy-atom interactions $\varepsilon_{XV}^{(n)}$ were fit to defect energies calculated from first-principles calculations. The vacancy-vacancy interactions $\varepsilon_{VV}^{(n)}$ have been estimated from empirical potentials.[30]

2. Kinetic parameters

The kinetic parameters include the saddle-point binding energies and the attempt frequencies. They have been fit to the iron self-diffusion coefficient[31] and the O (Ref. 32) impurity diffusion coefficient in iron. The yttrium diffusion coefficient in iron was also determined by fitting a classical nucleation-growth-coarsening model to small-angle neutron scattering data obtained by Allinger.[7] The experimental values are the following:

$$D_{Fe}^{Fe} = 6 \times 10^{-4} \exp\left(-\frac{2.91\ (\text{eV})}{k_B T}\right)(\text{m}^2\ \text{s}^{-1})$$

$$D_Y^{Fe} = 1 \times 10^{-5} \exp\left(-\frac{3.10\ (\text{eV})}{k_B T}\right)(\text{m}^2\ \text{s}^{-1})$$

$$D_O^{Fe} = 4 \times 10^{-5} \exp\left(-\frac{1.67\ (\text{eV})}{k_B T}\right)(\text{m}^2\ \text{s}^{-1}).$$

With these values, the yttrium diffusivity is approximately

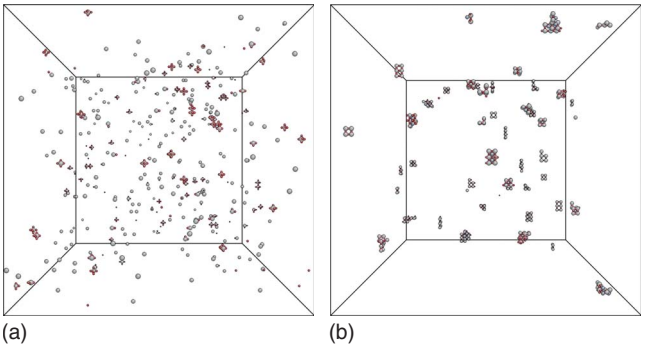

FIG. 4. (Color online) KMC simulation of Y_2O_3 homogeneous precipitation in Fe-0.12 at. %Y-0.18 at. %O (low supersaturation) during isothermal heat treatment at 1125 K. The simulation box is comprised of $100\times100\times100$ bcc cells. (a) 0.09 s, (b) 250 s. Yttrium atoms are the biggest, O atoms are the smallest.

400 times less than iron at 1125 K, while the oxygen diffusivity is about 3×10^5 times more rapid than iron.

III. RESULTS

In the simulation results presented here, the compositions and temperatures correspond to two-phase equilibrium states between α-Fe and Y_2O_3. The homogeneous precipitation in an Fe-0.12 at. %Y-0.18 at. %O alloy at 1125 K is described first. Next the results of using an anisothermal heat treatment with a temperature ramp rate of 20 K/min, up to 1125 K, are discussed to understand the role of the temperature ramp. A third simulation, with a higher supersaturation (Fe-0.25 at. %Y-0.37 at. %O alloy), is then presented to understand its influence on the kinetics of precipitation during an anisothermal heat treatment. In each simulation, a vacancy source/sink ensures that the equilibrium value for vacancy concentrations is maintained in both the isothermal or anisothermal heat treatments. The simulation boxes are comprised of $100\times100\times100$ bcc cells with full periodic boundary conditions.

It is important to note that the Y and O concentrations used in these simulations are consistent with those studied experimentally. Thus qualitatively valid results are expected from the KMC simulations for the different pathways derived from the various solute supersaturations and heat treatments.

A. Homogeneous precipitation during isothermal heat treatment

KMC simulations are performed for an iron solid solution with 0.12 at. % of yttrium and 0.18 at. % of oxygen at 1125 K. The evolution of the precipitate microstructure is shown in Figs. 4 and 5.

At very short times ($t\simeq10^{-5}$ s), a few dimers composed of one yttrium atom and one oxygen atom are observed, in addition to small precipitates [Figs. 5(a) and 5(b)]. The precipitates are principally composed of oxygen and iron atoms, as shown in Fig. 5(c). Around $t\approx3\times10^{-3}$ s, these metastable oxide precipitates grow until they reach a size of about

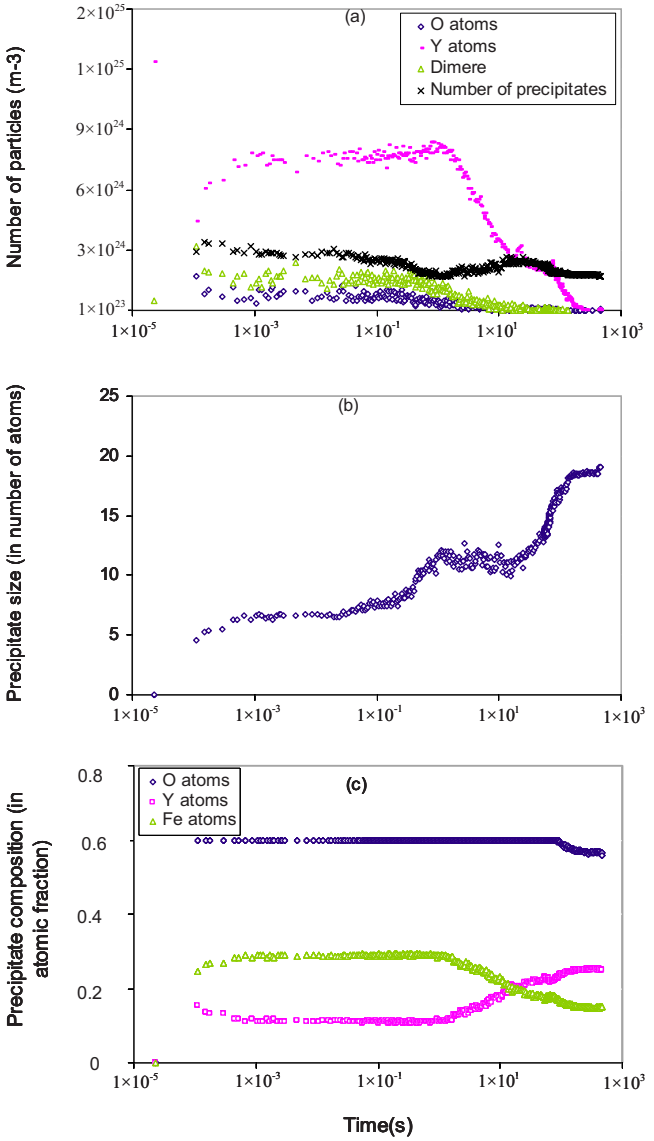

FIG. 5. (Color online) Monte Carlo simulation of homogeneous precipitation in Fe-0.12 at. %Y-0.18 at. %O (low supersaturation) during isothermal heat treatment at 1125 K. The simulation box is comprised of $100\times100\times100$ bcc cells. Evolution of: (a) number of particles (m^{-3}), (b) precipitate size (in number of atoms), and (c) precipitate composition (in atomic fraction).

ten atoms. Then, the coarsening stage takes place at $t\approx0.2$ s, with a decreasing number of precipitates. The transient formation of metastable oxides is ascribed to the rapid diffusion of oxygen atoms, which is approximately 10^8 times faster than yttrium, and to the existence of a driving force for iron oxide precipitation. While this clustering effect of oxygen to form metastable iron oxides seems intuitively understandable, the details of this metastable precipitation are certainly much more complex than the present model can account for. The composition and the crystalline structure of the metastable Fe_2O_3 oxides in this KMC model are *a priori* not correct. In an Fe-Y-O alloy, the transient precipitation of FeO could be expected, but its structure cannot be reproduced in the frame of this simple rigid lattice model, and the associated elastic energies due to lattice mismatch are not

accounted for. However, the clustering of oxygen before the precipitation of Y_2O_3 is probably valid. Similar metastable precipitation phenomenon was previously observed by Gendt[13] and Hin *et al.*[19] in KMC simulations of Fe-Nb-C alloys.

At $t \sim 1$ s, the number of dimers and the Y atoms in the bulk decrease. This corresponds to an observed transformation of the composition of the metastable Fe_2O_3 precipitate to Y enriched [Fig. 5(c)], along with a slight increase in the number of precipitates at roughly constant average size. This suggests the onset of nucleation of the stable Y_2O_3 phase. Different cases are envisaged to explain the observed nucleation: (1) Y_2O_3 precipitates nucleate in the bulk, (2) Y_2O_3 precipitates nucleate within the Fe_2O_3 precipitates, and (3) Y_2O_3 precipitates nucleate both in the bulk and at the Fe_2O_3 precipitates. The first case is not consistent with the observation that the average precipitate size remains constant instead of decreasing. The second case is more probable, however if the Y_2O_3 precipitates only nucleate within metastable Fe_2O_3 precipitates, then the density of precipitates should not increase. The third case is most likely. However, the increase in the precipitate number density (from 2.24×10^{24} to 2.45×10^{24} m^{-3}) is quite small, and thus it is logical to conclude that the Y_2O_3 precipitates nucleate preferentially within Fe_2O_3 precipitates and to a lesser extent, in the bulk. Consequently, the number of iron atoms that belong to precipitates (e.g., iron atoms that have in first neighbor at least four oxygen atoms belonging to a precipitate) decreases and the precipitate composition becomes more enriched in yttrium [Fig. 5(c)]. This new phase can be labeled $Fe_XY_{2-X}O_3$.

Between $t \sim 20$ and ~ 500 s, the number of precipitates remains approximately constant while the precipitate size increases and the Y content in the bulk decreases. It thus appears that the system has reached the growth stage. The composition of these precipitates continuously evolves during this stage with a decrease in Fe content and an increase in Y content, as shown in Fig. 5(c), and is expected to ultimately approach the stoichiometric composition of Y_2O_3.

At the end of the simulation, which consists of 500 s of isothermal heat treatment at 1125 K, there are about 2.1×10^{24} m^{-3} $Fe_XY_{2-X}O_3$ precipitates (with $X \approx 0.5$) with an average size of ~ 20 atoms (≈ 0.54 nm). The kinetic path of the stable Y_2O_3 phase seems to be

$$Fe_2O_3 \rightarrow Fe_XY_{2-X}O_3 \rightarrow Y_2O_3.$$

B. Homogeneous precipitation during anisothermal heat treatment

1. Low supersaturation

A KMC simulation was then performed to study the evolution of an iron solid solution with 0.12 at. % of yttrium and 0.18 at. % of oxygen during an anisothermal heat treatment, with a temperature heating rate of 20 K/min, up to 1125 K. The KMC simulation begins at 600 K, since there is little diffusion or microstructural evolution below this temperature. The evolution of the precipitate microstructure is shown in Figs. 6 and 7. A comparison with Figs. 5–7 reveals

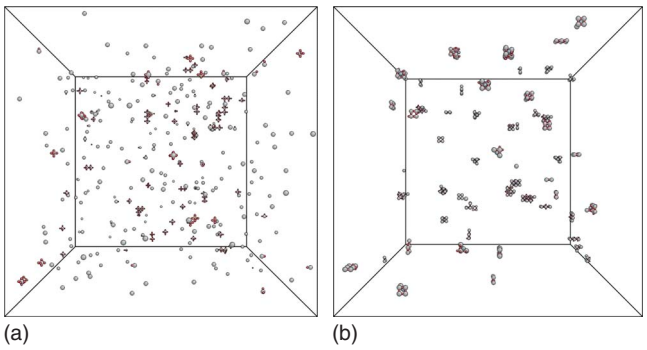

FIG. 6. (Color online) KMC simulation of Y_2O_3 homogeneous precipitation in Fe-0.12 at. %Y-0.18 at. %O (low supersaturation) during anisothermal heat treatment. The temperature ramp rate is equal to 20 K/min, up to a maximum temperature of 1125 K. The simulation box is comprised of $100 \times 100 \times 100$ bcc cells. (a) 983 s, (b) 1547 s. Yttrium atoms are the biggest, O atoms are the smallest.

a different precipitation kinetics for the anisothermal heat treatment.

At the beginning of the heat treatment ($t \simeq 10^{-1}$ s), when the temperature first begins to increase, there is a decrease in the solute atoms in solid solution, leading to the formation of dimers and small precipitates [Figs. 7(a) and 7(b)]. The dimers are three times more numerous than in the isothermal case, as shown in [Fig. 5(a)], and are composed of one yttrium atom and one oxygen atom. The small precipitates are principally composed of oxygen and iron atoms [Fig. 7(c)] and appear for the same reason as previously discussed. After 10 s, the number of dimers remains relatively constant, while the number of precipitates continues to increase and the precipitate size remains constant.

After 300 s, the temperature is now 700 K and still increasing by 20 K/min. Both the number of precipitates and the number of dimers decrease significantly while the number of yttrium atoms in the solid solution increases. This can be understood due to the decreasing driving force of nucleation and the increasing critical radius of the precipitate with increasing temperature. This drives to the dissolution of small precipitates and dimers, which are now smaller than the critical precipitate size. At the same time, Fe_2O_3 precipitates, which are larger than the critical size, continue to grow, due to the faster diffusion of oxygen atoms released from the dissolved precipitates and Y-O dimers.

Between $t \sim 900$ and ~ 1100 s (corresponding to an increase temperature from 864 K to 963 K), the number of precipitates decreases while the precipitate size rapidly increases. This is ascribed to the fact that two phenomena occurring simultaneously: (i) the coarsening stage of Fe_2O_3 precipitates above the critical radius and (ii) the dissolution of precipitates that are now smaller than the critical size of precipitates, which continues to increase with the temperature.

At $t \sim 1100$ s of anisothermal heat treatment, both the number of yttrium atoms in the solid solution and the precipitate size decreases, while the number of precipitates increases. Moreover, the precipitate composition becomes more enriched in yttrium [Figs. 7(c) and 7(g)]. This observa-

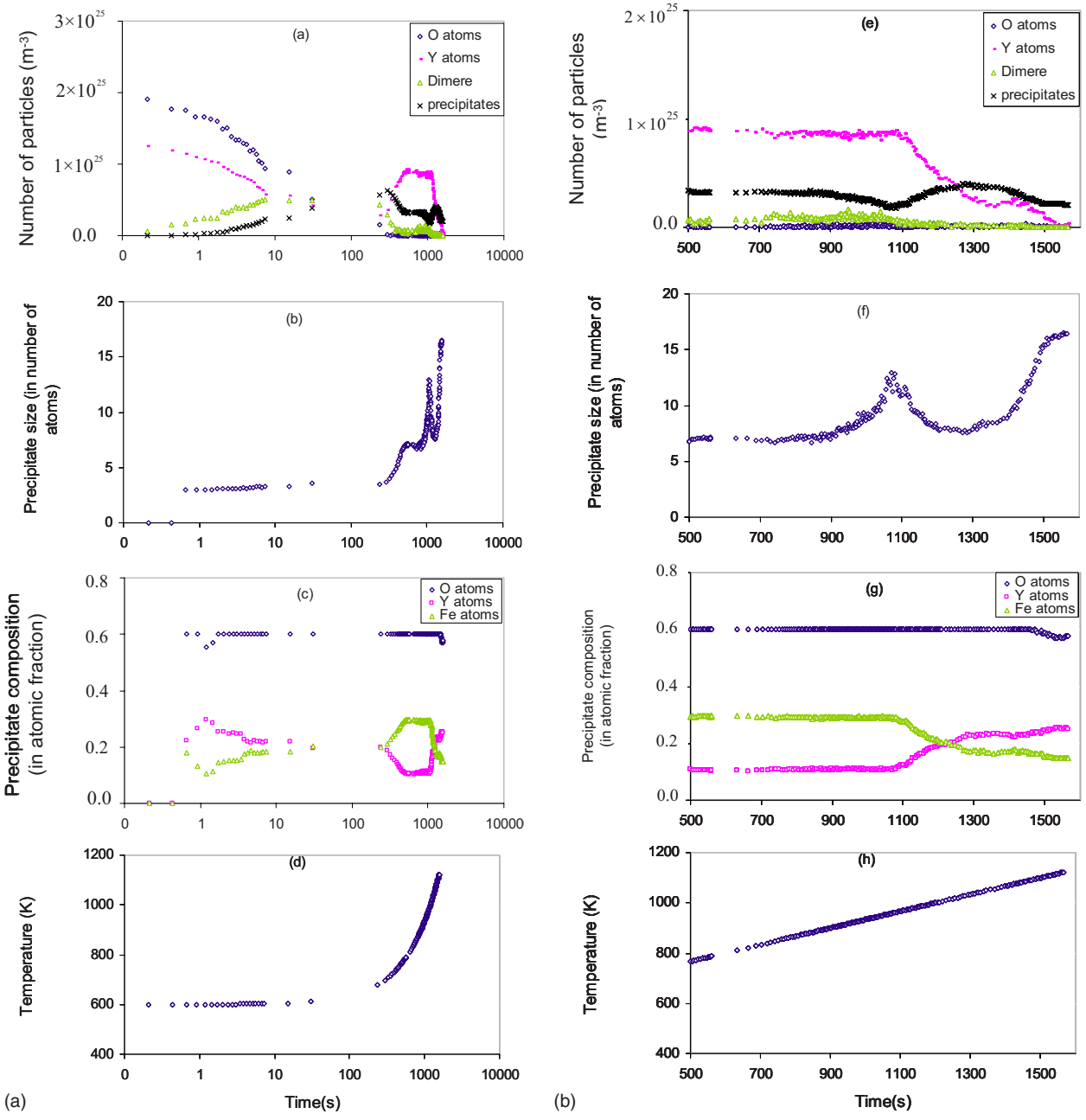

FIG. 7. (Color online) Monte Carlo simulations of homogeneous precipitation in Fe-0.12 at. %Y-0.18 at. %O (low supersaturation) during an anisothermal heat treatment. The temperature ramp rate is equal to 20 K/min, up to a maximum temperature of 1125 K. The simulation box is comprised of $100\times100\times100$ bcc cells. Evolution of: (a) number of particles (m^{-3}), (b) precipitate size (in number of atoms), (c) precipitate composition (in atomic fraction), and (d) temperature as a function of time. In order to better understand the computed behavior, which shows many different regime between 500 and 1500 s, Figs. 6(a)–6(d) have been plotted Figs. 6(e)–6(h), between 500 and 1500 s with a nonlogarithmic scale.

tion corresponds to the nucleation of Y_2O_3 precipitates that are enriched in iron, due to the fact that the Y_2O_3 precipitates mainly nucleate within the Fe_2O_3 precipitates and to a lesser extent in the bulk.

Between $t\sim1300$ and ~1400 s, the number of $Fe_XY_{2-X}O_3$ precipitates remains constant while the precipitate size increases, and the Y content decreases in the solid solution. The system has reached the growth stage of the $Fe_XY_{2-X}O_3$. At the end of this stage, the precipitates are more enriched in Y with $X\approx1$.

Finally, at $t\sim1400$ s the number of $Fe_XY_{2-X}O_3$ precipitates decreases due to the existence of a capillary driving force that tends to minimize the free surface energy of the system. At the same time, the precipitate size still increases and the composition of the precipitates continuously evolves with a decrease in Fe content and an increase in Y content, as shown in [Figs. 7(c) and 7(g)], and approaches the stoichiometric composition of Y_2O_3.

At the end of this simulation after 1500 s of anisothermal heat treatment, the temperature plateau at 1125 K is reached.

Approximately 3.0×10^{24} m^{-3} $Fe_XY_{2-X}O_3$ (with $X\approx0.5$) precipitates have formed with an average size of ~18 atoms (≈0.52 nm). It is important to note that the density of precipitates obtained by KMC simulations is of the same order of magnitude than those obtained experimentally, although the size is slightly smaller. Once again, the observed kinetic path of the Y_2O_3 precipitation is

$$Fe_2O_3 \rightarrow Fe_XY_{2-X}O_3 \rightarrow Y_2O_3,$$

Comparison of the isothermal and anisothermal temperature history in the KMC simulations reveals an effect of the treatment history on the kinetic path of precipitation. Notably, the formation and dissolution of Fe_2O_3 can only be observed during an anisothermal heat treatment due to the decreasing driving force of nucleation and the increasing critical radius of the precipitate with increasing temperature. The treatment history can also have an effect on the size and number density of the precipitates.

This difference in size and density can be noticed by comparing the precipitate distribution after 500 s, the precipitate size is considerably smaller in the anisothermal heat treatment than during an isothermal heat treatment (seven atoms for the anisothermal heat treatment case at 765 K versus 19 atoms per precipitates for the isothermal heat treatment at 1125 K). Correspondingly, the number density is at least four times larger during the anisothermal treatment. On the other hand, the precipitate distributions are more comparable when comparing at the same temperature (e.g., at the end of the temperature ramp), when the density of precipitates is around 2×10^{24} m^{-3} and the precipitate size consists of between 16 and 20 atoms, regardless of the heat treatment. Nevertheless, the anisothermal heat treatment seems to favor the formation of numerous smaller precipitates since the maximum of precipitate density is 6×10^{24} m^{-3} for an average size of precipitates equal to seven atoms per precipitates during the anisothermal case while the maximum of precipitate density is only 2.3×10^{24} m^{-3} for an average size of precipitates equal to 11 atoms per precipitates in the isothermal case.

2. High supersaturation

KMC simulations have also been performed to study the evolution of an iron solid solution with 0.25 at. % of yttrium and 0.37 at. % of oxygen during the anisothermal heat treatment. The temperature history is the same as described in Sec. III B 1. The evolution of the precipitate microstructure is shown in Fig. 8. Since the solid solution is more supersaturated than in the previous case, the KMC simulation is more computationally efficient and the system reaches the temperature plateau of 1125 K. However, comparison between Figs. 7 and 8 show that the kinetic precipitation path is similar. At the end of the simulation, after 2200 s, there are approximately 4.2×10^{24} m^{-3} $Fe_XY_{2-X}O_3$ (with $X\approx0.5$) precipitates [Fig. 8(a)], with an average size of ~16 atoms (≈0.50 nm) [Fig. 8(b)]. The composition of the precipitates continuously evolves with a decrease in Fe content and an increase in Y content, as shown in Fig. 8(c), until approaching the stoichiometric composition of Y_2O_3.

The only significant difference between the two anisothermal heat treatment KMC simulations is in the number and size of the precipitates. For example, when the temperature plateau of 1125 K is reached, the number of precipitates is about 1.5 times more numerous and the size of precipitates is

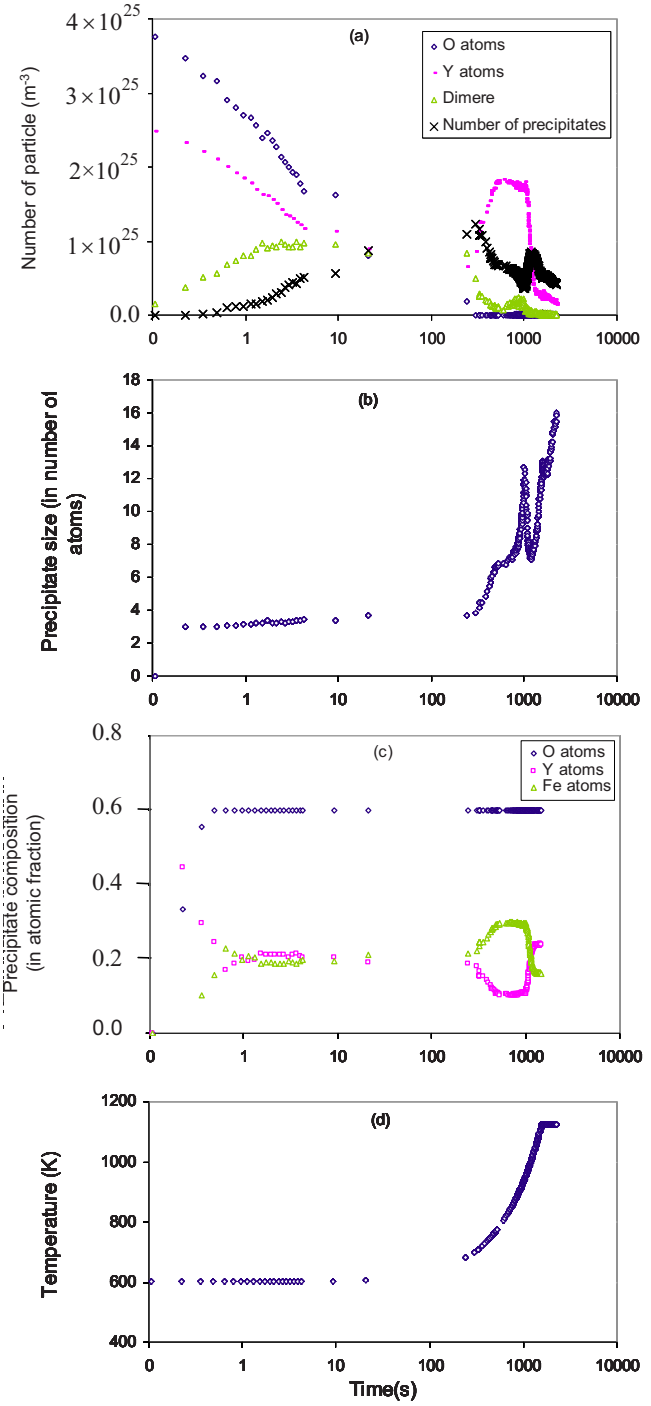

FIG. 8. (Color online) Monte Carlo simulation of homogeneous precipitation in Fe-0.25 at. %Y-0.37 at. %O (higher supersaturation) during an anisothermal heat treatment. The temperature ramp rate is equal to 20 K/min, up to a maximum temperature of 1125 K. The simulation box is comprised of $100\times100\times100$ bcc cells. Evolution of: (a) number of particles (m^{-3}), (b) precipitate size (in number of atoms), (c) precipitate composition (in atomic fraction), and (d) temperature as a function of time.

1.5 times smaller for the higher supersaturated solid solution (Figs. 7 and 8).

Thus, both KMC simulations of anisothermal heat treatments reveal that the degree of supersaturation does influence the density and size of precipitates at comparable aging times, but does not significantly impact the kinetic pathway of precipitation.

IV. CONCLUSIONS

Kinetic Monte Carlo simulations, using a residence time algorithm, are well suited for studying general nucleation problems and have been extended to an anisothermal heat treatment history. Kinetic Monte Carlo simulations have been used to investigate Y_2O_3 precipitation in α iron during isothermal and anisothermal heat treatment and reveal a significant effect of the heat treatment on the kinetic path of precipitation. However, in both cases, there is the initial formation of a transient, metastable iron oxide phase, which forms due to the rapid diffusion of oxygen relative to yttrium, and due to the existence of a driving force for iron oxides precipitation. For isothermal heat treatment, the formation of Fe_2O_3 is followed by the nucleation Y_2O_3 precipitates, which occurs within the Fe_2O_3. The phase, called $Fe_XY_{2-X}O_3$, subsequently grows with a decrease in Fe content and an increase in Y content. On the other hand, during an anisothermal heat treatment, a large number of very small Fe_2O_3 precipitates and Y-O dimers form during the initial stage of the temperature ramp. Then, the growth and coarsening stages of Fe_2O_3 precipitates take place. As the temperature increases, the driving force of nucleation decreases and the critical precipitate radius increases. Consequently, the small iron-oxides precipitates and dimers dissolve. This leads to an acceleration of the coarsening stage. Finally, the nucleation of Y_2O_3 precipitates mainly occurs within the Fe_2O_3 precipitates. This stage is followed by the growth and coarsening type reaction of the $Fe_XY_{2-X}O_3$ precipitates, which are more and more enriched in Y. An effect of the heat treatment can also be observed looking at the size and number density of the precipitates. A higher density of smaller precipitates appears during the anisothermal heat treatment. Thus, it appears that careful choice of the anisothermal heat treatment can provide a means to control the number density and size of nanoscale Y_2O_3 precipitates and correspondingly, the creep strength, which is an important mechanical property to optimize within these alloys for high temperature service conditions. Finally, the degree of supersaturation does not appear to significantly affect the kinetic path of precipitation, but higher supersaturation does also favor a higher density of smaller precipitates.

ACKNOWLEDGMENTS

We gratefully acknowledge useful and stimulating discussions with Y. Bréchet, W. C. Carter, and A. Simar. The authors gratefully acknowledge the financial support of the National Science Foundation under Contract No. NSF DMR 0548259 and the Department of Energy, Office of Fusion Energy Sciences under Grant No. DE-FG02-04GR54750. Portions of this work were performed at the Molecular Foundry, Lawrence Berkeley National Laboratory, which is supported by the Office of Science, Office of Basic Energy Sciences, of the U. S. Department of Energy under Contract No. DE-AC02-05CH11231.

[1] S. Ukai and M. Fujiwara, J. Nucl. Mater. **307-311**, 749 (2002).
[2] R. Lindau, A. Moeslang, M. Schirra, P. Schlossmacher, and M. Klimenkov, J. Nucl. Mater. **307-311**, 769 (2002).
[3] J. Bertsch, R. Lindau, and A. Moeslang, J. Nucl. Mater. **233-237**, 276 (1996).
[4] G. R. Odette and G. E. Lucas, J. Nucl. Mater. **179-181**, 572 (1991).
[5] N. Miyaji, Y. Abe, S. Ukai, and S. Onose, J. Nucl. Mater. **271-272**, 173 (1999).
[6] I. Monnet, Ph.D. thesis, Ecole Centrale de Paris, 1999.
[7] M. Alinger, Ph.D. thesis, University of Santa Barbara, 2004.
[8] C. Hin, Ph.D. thesis, Institut National Polytechnique de Grenoble, 2005.
[9] C. Hin, F. Soisson, P. Maugis, and Y. Bréchet, *Solid-Solid Phase Transformation in Inorganic Materials* (TMS, Phoenix, AZ, 2005), Vol. 2, p. 771.
[10] C. Hin and B. D. Wirth, J. Nucl. Mater. (to be published).
[11] B. H. O'Connor and T. M. Valentine, Acta Crystallogr., Sect. B: Struct. Crystallogr. Cryst. Chem. **25**, 2140 (1969).
[12] A. Deschamps and Y. Bréchet, Acta Mater. **47**, 293 (1998).
[13] D. Gendt, Ph.D. thesis, Université de Paris XI, 2001.
[14] F. Perrard, A. Deschamps, and P. Maugis, Acta Mater. **55**, 1255 (2007).
[15] T. S. King, in *Surface Segregation Phenomena*, edited by P. A. Dowben and A. Miller (CRC, Boca Raton, 1990).
[16] P. Bellon and G. Martin, Mater. Sci. Forum **155-156**, 209 (1994).
[17] W. M. Young and E. W. Elcock, Proc. Phys. Soc. London **89**, 735 (1966).
[18] Y. LeBouar and F. Soisson, Phys. Rev. B **65**, 094103 (2002).
[19] C. Hin, Y. Bréchet, P. Maugis, and F. Soisson, Acta Mater. **56**, 5653 (2008).
[20] J. P. Perdew and A. Zunger, Phys. Rev. B **23**, 5048 (1981).
[21] D. Vanderbilt, Phys. Rev. B **41**, 7892 (1990).
[22] G. Kresse and J. Furthmuller, Comput. Mater. Sci. **6**, 15 (1996).
[23] H. J. Monkhorst and J. D. Pack, Phys. Rev. B **13**, 5188 (1976).
[24] J. D. Pack and H. J. Monkhorst , Phys. Rev. B **16**, 1748 (1977).
[25] G. Inden, Acta Metall. **22**, 945 (1974).
[26] F. Ducastelle, *Order and Phase Stability in Alloys* (North-Holland, Amsterdam, 1991).
[27] O. Kubaschewski, *Iron-Binary Phase Diagrams* (Springer, Berlin, 1982).
[28] H. K. D. H. Bhadeshia, Mater. Sci. Technol. **14**, 273 (1998).
[29] P. J. Spencer and O. Kubashewski, CALPHAD: Comput. Coupling Phase Diagrams Thermochem. **2**, 147 (1978).
[30] R. A. Johnson, Phys. Rev. **134**, A1329 (1964).
[31] A. Seeger, Phys. Status Solidi A **167**, 289 (1998).
[32] R. Barlow and P. J. Grundy, J. Mater. Sci. **4**, 797 (1969).